Ultraviolet Sensing Using TiO_2 Nanotube Integrated High Resolution Planar Microwave Resonator Device

Mohammad H. Zarifi[1†], Benjamin Wiltshire[2], Najia Mahdi[2], Karthik Shankar[2†] and Mojgan Daneshmand[2†]

[1]School of Engineering, University of British Columbia, Canada, V1V 1V7

[2]Department of Electrical and Computer Engineering, University of Alberta, Canada, T6G 1H9

† Corresponding authors' E-mail: mohammad.zarifi@ubc.ca, kshankar@ualberta.ca, Daneshmand@ualberta.ca.

This paper presents a unique integrated UV light sensing concept and introduces a device with a detection limit of 1.96 nW cm^{-2}. The combination of a high quality factor, microwave planar resonator (Q ~ 50,000) with a semiconducting nanomaterial, enables a revolutionary potential paradigm for photodetection of low light intensities and small form factors. The presenting device employs a high-resolution microwave microstrip resonator as the signal transducer to convert the variant dielectric properties (permittivity and conductivity) of the nanotube membrane into electrical signals such as resonant frequency, quality factor and resonant amplitude. The microwave resonator has an active feedback loop to improve the initial quality factor of the resonator from 200 to 50,000 and leads to boosting the sensing resolution by orders of magnitude. Anatase TiO_2 nanotubes are assembled on the surface of the microwave resonator. Upon exposure to UV light, electron-hole pair generation, trapping and recombination in the nanotubes are exploited as the unique signature to quantify the UV light intensity. The change of dielectric properties in the nanotube membrane is monitored by the underlying active microwave resonator. The proposed concept enables detection and monitoring of UV light at high resolution, with very small exposure power and integrated form factors.

Keywords: optoelectronic device, microwave photoconductivity, split ring resonator, metamaterial, electrochemical anodization, freestanding membrane

Electronic Supplementary Information (ESI) available. See DOI: 10.1039/x0xx00000x.

1 Introduction

Microwave sensors have become more and more popular for both lab-scale and industrial scale applications. They can be used for distance measurement,[1] particle size classifications,[2] movement and shape detection and material identification.[3] Microwave sensors operate based on electric field variation in their close vicinity which gives them the advantage of contactless sensing. An alteration in the electric field around the sensor is produced by dielectric property variation of the analyte which is then detected to provide sensing action.

Among the different types of microwave sensors, planar microwave microstrip sensors demonstrate more attractive and robust performance since they have simple, inexpensive, stable, and easy to implement structure.[4, 5] A combination of a resonance phenomenon with a planar microwave microstrip device can result in a sensor device with higher accuracy and selectivity to the dielectric property in comparison to the other counterparts. In a planar microwave resonator device - resonant amplitude, resonant frequency and quality factor are three parameters (of which two are independent) which can be monitored as indicators for dielectric property variation in the resonator's environment. The planar microwave resonators can easily be combined with microfluidics techniques, microbeads and nanostructures for different sensing purposes. Wang *et al* recently reported a microwave capacitor sensor array based on microstrip band-stop filters, for proximity detection of different objects. They showed a significant improvement in quality factor using metamaterial split-ring structures coupled to a microstrip line in comparison to conventional surface-mounted or microstrip meander inductors.[6] Benkhaoua *et al* presented a novel miniaturized sensor based on a planar, double-sided spiral split-ring resonator for liquid concentration measurements and demonstrated that a strong electric field can be established at the resonant frequency on a sensor's hotspots thus enabling an accurate measurement of concentration in the liquid phase.[7] We have previously reported on carrier dynamics studies, monolayer sensing and selective chemical sensing using TiO_2 nanotube membranes integrated with planar microwave resonators and illuminated by photons of different wavelengths.[8-10] However, these prior studies used low-to-medium *Q*-factor resonators while the present report uses a high *Q*-factor resonator and advances a new concept for photodetection involving the synergistic action of a semiconductor nanomaterial and a microwave resonator.

While planar microwave resonators have demonstrated several advantages in sensing applications, they suffer from low resolution in sensing the dielectric property variation in their near environment. The resolution of a sensor with a second order response can be described by the minimum detectable resonant frequency and is mainly related to the -3 dB quality factor of the resonant profile as presented in equation (1):[11, 12]

$$\Delta f_m = \Delta A \frac{3\sqrt{3}\,k}{2A_0 Q} \qquad (1)$$

where Δf_m is the minimum detectable frequency variation, ΔA is the noise signal amplitude, A_0 is the amplitude of the response profile at the resonant frequency and Q is the -3 dB quality factor of the profile.

According to equation (1), increasing the quality factor improves the signal to noise ratio and reduces the minimum detectable resonant frequency shift, concomitantly enhancing the resolution of the sensor in detecting permittivity variations.[12] Q-factor is merely a measure of the energy stored in a resonator per unit cycle to the energy dissipation rate. Therefore, in order to increase the quality factor of a planar resonator, the loss in the structure should be compensated by an active feedback loop around the passive structure.[13] The authors have previously shown that the regenerative feedback loop can enhance the quality factor by orders of magnitude without any destructive effect on the sensitivity of the sensor by pumping back the lost energy to the loop using active devices such as transistors.[11, 12] The quality factor enhancement not only improves the resolution of the sensor device but also increases the penetration depth of electric field around the resonator and enables contactless sensing at large distances.[14, 15]

Titanium dioxide (TiO_2) nanotube arrays are useful for light detection due to their wide bandgap (3.0 eV for rutile phase, 3.2 eV for anatase phase).[16] TiO_2 nanotubes allow enhanced light-matter interactions through photonic crystal, Mie scattering and metamaterial effects.[17-21] The high surface area to volume ratio also allows the insides and walls of the nanotubes to be coated with light-sensitive dyes or quantum dots, enabling them to detect light outside the UV spectrum if desired through the process of sensitization. The nanotube arrays are easy to work with and have well studied growth mechanisms, including growth methods that allow the nanotube arrays to detach from the substrate to form a porous membrane.[22-24] Titanium dioxide also has well studied UV absorption and permittivity properties in the X-band region; the kinetics of charge excitation

and trapping are also becoming better understood as they are continually studied.[25-32] Furthermore, TiO_2 is a relaxation semiconductor as opposed to a lifetime semiconductor. This means that the majority carriers and minority carriers can be engineered to have differing lifetimes in TiO_2 (instead of a single ambipolar lifetime in say Si) through a high capture cross-section of deep level traps for holes while simultaneously ensuring a low reactivity of photogenerated electrons with trapped holes. Due to the trap-mediated suppression of recombination, mobility-lifetime ($\mu\tau$) products as high as 2×10^{-4} m^2V^{-1} are achievable in monocrystalline TiO_2 nanorod arrays,[33] which in turn translates into a high photoconductive gain G since $G \alpha \mu\tau$.

Here in this work, a high-resolution microwave planar resonator integrated with a TiO_2 nanotube membrane is presented for detection of ultra-low intensity of UV light. UV light sensing is necessary in both commercial and military applications such as HPLC, space-to-space communication, flame detection, water purification, pollution monitoring, and UV-sensitive food or drug packaging.[34, 35] Highly sensitive light sensing is necessary when the signal of interest is weak, possibly due to a lossy transfer medium or a long travel distance. Additionally, using a less powerful signal that still lies within the range of detection could improve the efficiency of the UV systems. Previously, material detection methods based on manipulating the band energy of ZnO, diamond, SiC, or other wide bandgap materials have been used.[36-45] TiO_2 nanotubes are also useful because of the wide range of UV energy they can detect without using filters to stop low energy photons.

2 Theory of Operation and Finite Element Simulations of Microwave Resonator

A planar microwave ring resonator assisted with a regenerative feedback loop is designed and simulated in HFSS software. The main core of the structure is a ring resonator which is magnetically coupled to the input and output signal lines. The length of the resonator and the loop capacitor determine the resonant frequency of the passive resonator. Fig. 1a. presents the resonator structure and the dimensions for each section. A comparison between resonant profiles, which are S_{21}-parameters, is presented in Fig. 1b. The passive resonator exhibits a quality factor of 250

whereas the active resonator (passive structure with regenerative feedback) exhibits a loaded quality factor of 48,520.

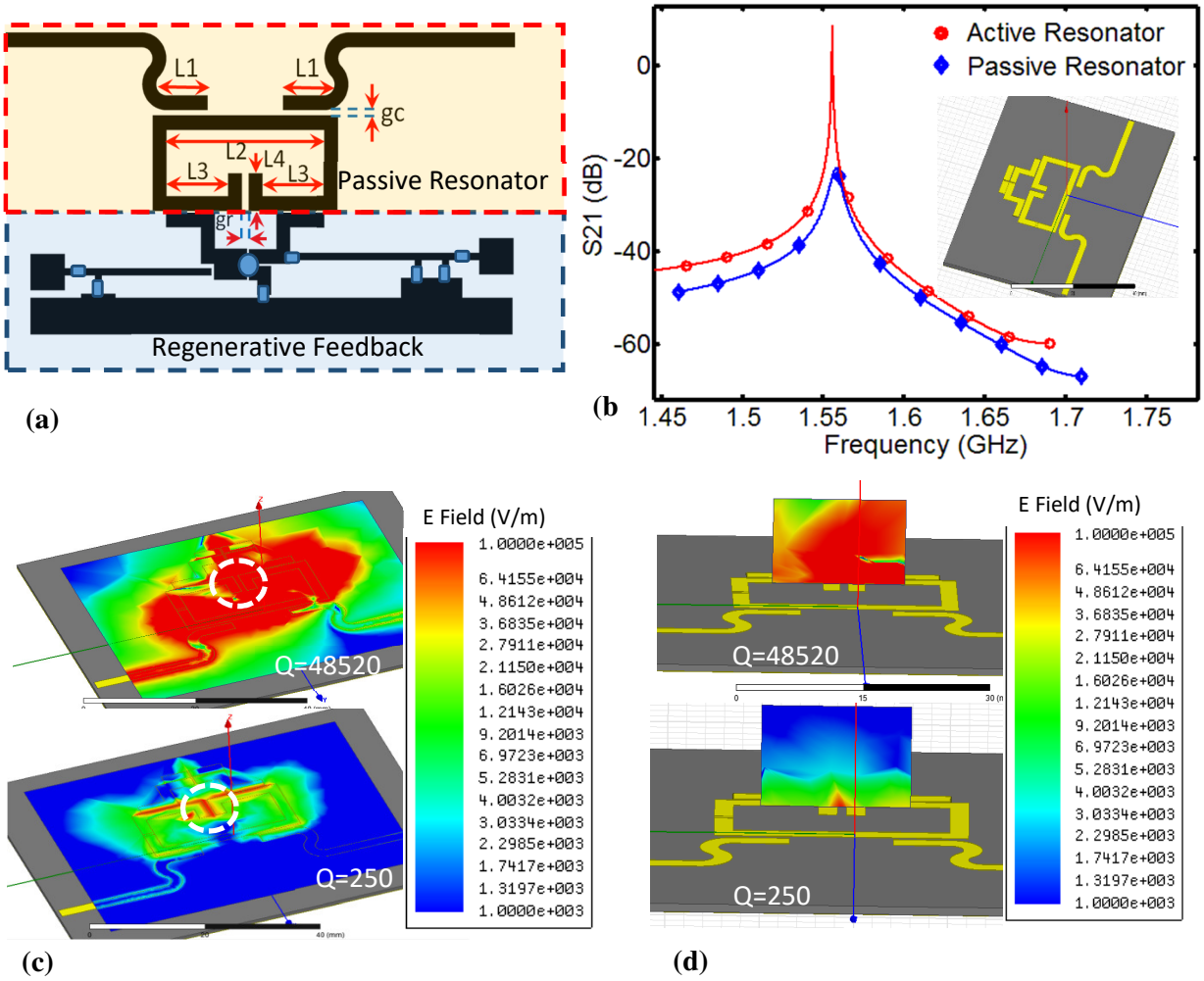

Fig. 1 (a) Resonator structure with passive loop and active feedback for loss compensation (b) Comparison of resonant profiles (S21-parameter) of the resonator in active and passive state (c) In-plane electric field comparison for active and passive resonator and (d) Electric field penetration in a plane perpendicular to the resonator surface.

As shown in Fig. 1c and Fig. 1d, active feedback around the passive resonator structure enhances the electric field in the resonant loop, as well as in front of the resonator with distance from its surface. The enhanced electric field around the resonator improves the signal to noise ratio and enables detection of very small variations in the electrical properties (permittivity and conductivity) of materials in the sensor medium. The implemented size of the sensor structure in Fig. 1a is presented in Table I. The electrical parameters of Rogers 5880 radio frequency substrate

with dielectric thickness of 0.78 mm and copper metal conductor thickness of 0.035mm is used for HFSS simulation.

Table 1. Summary of geometrical factors (indicated in Fig. 1a) for the implemented sensor structure.

	L_1	L_2	L_3	L_4	g_c	g_r	W
(mm)	8	23.2	9.1	5.1	0.8	0.9	1.9

To demonstrate the performance of the active microwave planar resonator sensor with respect to variant permittivity and loss tangent of the near medium, a material under test (MUT) is placed in the most sensitive region of the resonator structure. The physical size of MUT is (3 mm × 3.8 mm × 0.017 mm) and its initial permittivity and conductivity are set to 10.1 and 0, respectively. Fig. 2a presents the sensor with MUT in the resonant gap (HFSS software) while Fig. 2b illustrates the sensor's resonant behaviour with respect to a change in the dielectric properties of the MUT material.

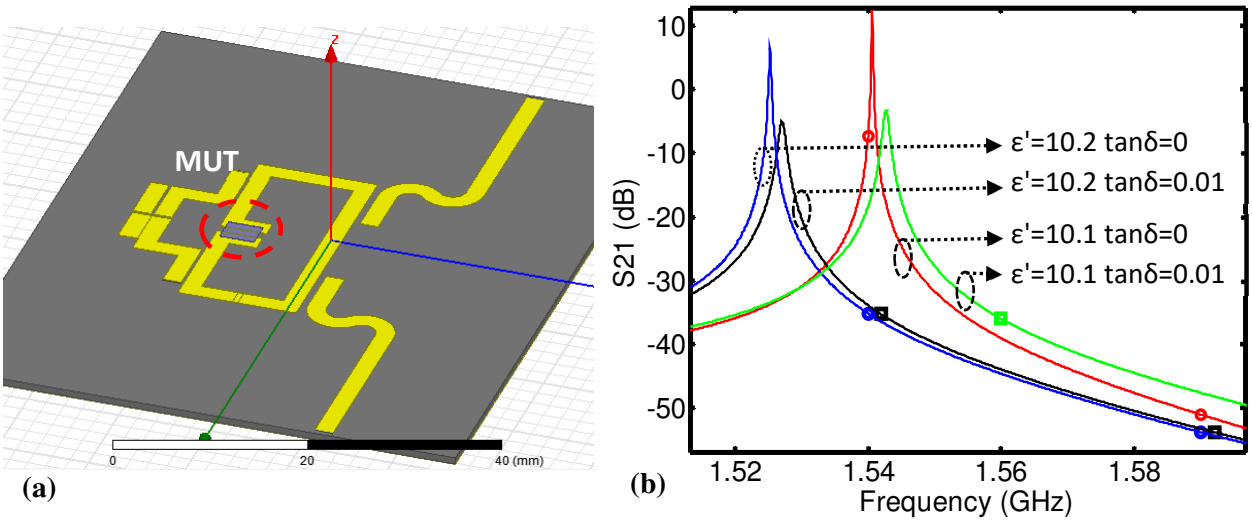

Fig. 2 (a) Sensor structure with MUT in the resonant gap implemented in HFSS simulator and (b) Resonant profile change (S_{21}-parameter) as a response to permittivity and loss tangent variation in the MUT material.

3 Experimental Results and Discussion

Ultraviolet illumination intensity measurements were performed in a dark room with controlled environmental parameters such as relative humidity and temperature. As shown in Fig. 3, a constant current drove a UV-LED (390 nm) which was mounted out of a plastic chamber with a quartz window. The bias current of the UV-LED was controlled by a Keithley semiconductor parameter analyzer, which was being controlled remotely and was used to adjust the intensity level of the UV-LED. A direct current (DC) bias source provided the voltage supply to the active circuit of the microwave resonator sensor and a vector network analyzer (VNA) equipped with LabVIEW program measured the sensor's response in the time domain. The VNA was NIPXI 1075 with IF bandwidth set to 300 Hz, number of points at 2001, and microwave output power of -15 dBm. The sensor's output profile was measured every 10 seconds. To eliminate any thermal conduction/convection related heating effects from the light source on the nanotube membrane and on the microwave resonator device, the UV-LED was placed out of the plastic chamber. Prior to the microwave experiment, the intensity of the UV-LED at different levels of bias current, was measured using a commercially available UV detector (Thorlabs), and the same bias currents were applied during the experiments. Broadband multilayer microwave signal absorber foams (ECCOSORB AN-79) were placed all around the sensor and the network analyzer to reduce any interference and unwanted noise effects on the sensor.

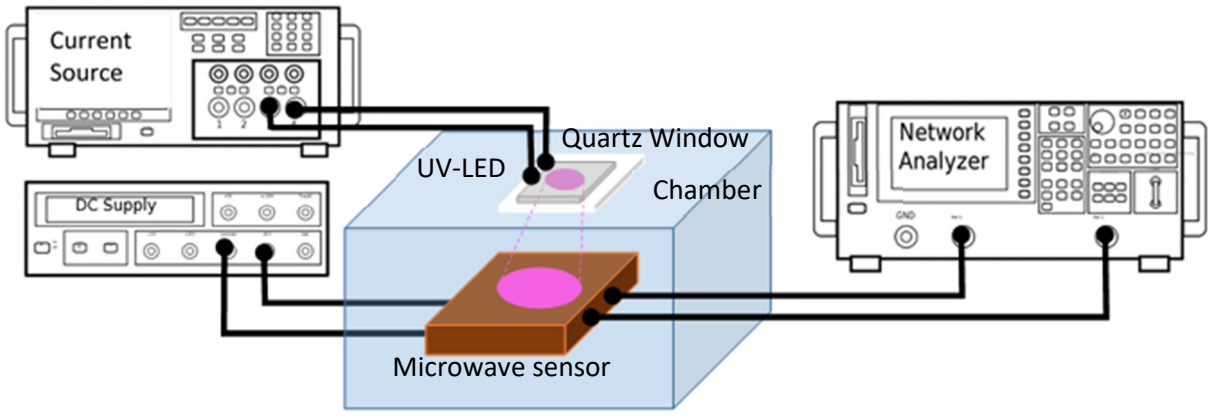

Fig. 3 Schematics of the experimental setup for the UV-Intensity measurement using TiO_2 nanotube membrane enforced microwave high-resolution resonator sensor.

The implemented sensor structure and TiO_2 nanotube membrane is shown in Fig. 4a. The resonant profile (S_{21} scattering parameter) of the sensor prior to illumination is shown in Fig. 4b. According to the presented profile, the maximum amplitude of the resonant profile is defined as the resonant amplitude and the frequency associated with that amplitude is defined as the resonant frequency. The bias current of the UV-LED was set to 3 mA (associated with an intensity of 4.56 $\mu W/cm^2$) for a time period of 9600 seconds. Both resonant frequency and amplitude were recorded during the time using LabVIEW program and VNA device (Fig. 4c and Fig. 4d).

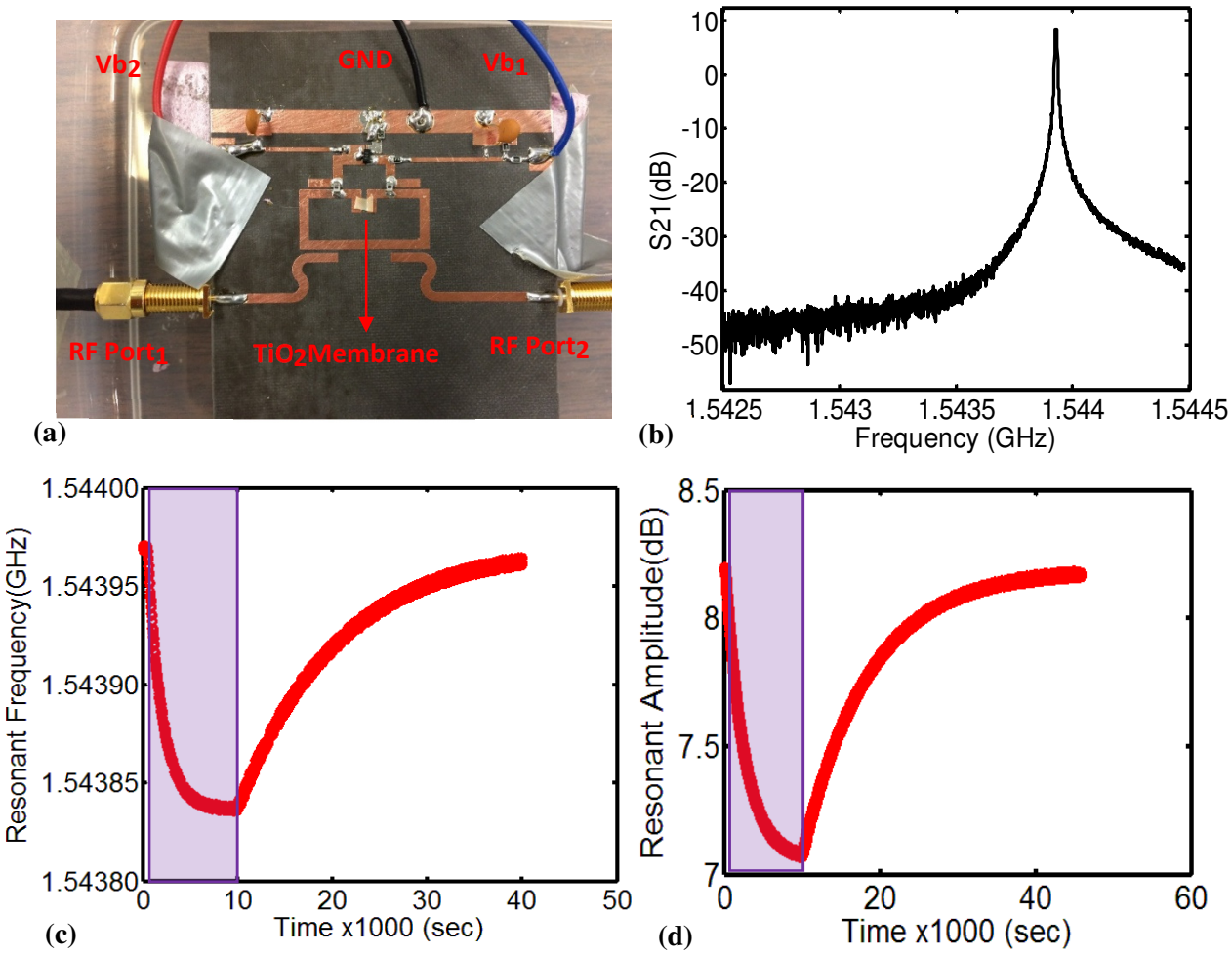

Fig. 4 (a) Fabricated microwave sensor and TiO_2 membrane placed in the sensing chamber (b) S21- parameter profile of the sensor with membrane prior to illumination (c) Resonant frequency versus time during the illumination and relaxation time period and (d) Resonant amplitude versus time during the excitation and the relaxation time.

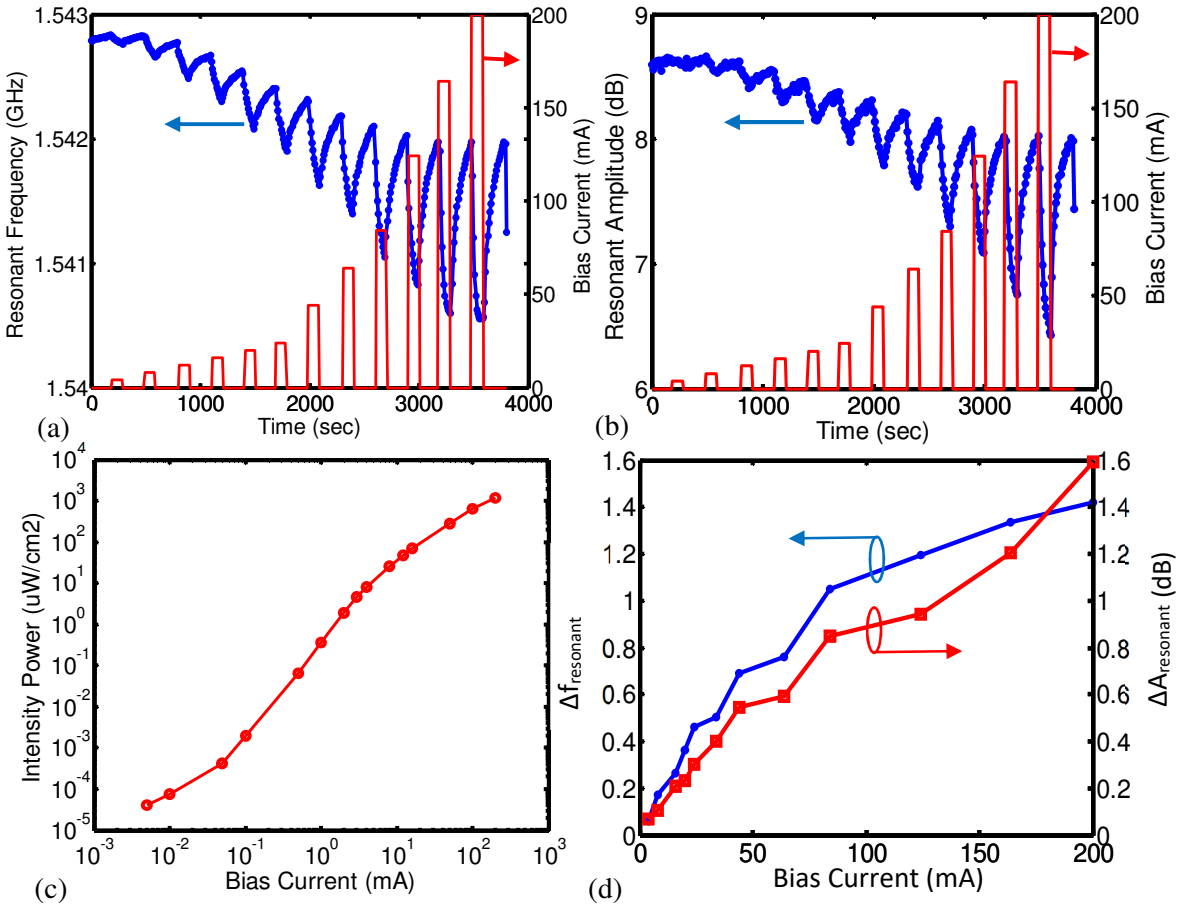

Fig. 5 (a) Transient response of the resonant frequency for a step change in bias current of the UV-LED (b) Resonant amplitude response to the step change in the bias current, (c) Intensity power incident from the UV-LED on the sample plotted for different bias current levels and (d) Resonant frequency change ($\Delta f_{resonant}$) and resonant amplitude change versus($\Delta A_{resonant}$) bias current of the UV-LED regarding to the dark medium condition.

The transient resonant frequency (in GHz), (Fig. 4c) was fitted to $f_r(t) = 1.543 + 0.172e^{-(t-100)/1537}$ for the excitation part and $f_r(t) = 1.5439 + 0.329e^{-(t-100)/10495}$ for the relaxation part. The resonant amplitude variation versus time in Fig. 4d, was also perfectly matched to the following first order exponential curve for the excitation period, $A_r(t) = 7.06 + 1.187e^{-(t-100)/2397}$, while for the relaxation period the response was fitted to $A_r(t) = 8.19 - 3.393e^{-(t-500)/8508}$. A step-illumination experiment was performed on the TiO_2 membrane placed on the microwave sensor where the resonant frequency and amplitude variation versus time at different bias current levels were measured. The illumination time for each current level was 100 s and the relaxation time was 200 s (Fig. 5a and Fig. 5b). As shown in Fig. 5c, each bias current represents a different intensity level, which was measured by a commercially available photodiode

(Thorlabs SM1PD2A). For the step response experiments, the bias current was changed from 4 mA to 200 mA which was associated with the intensity power variation from 7.94 μW cm^{-2} to 1204 μW cm^{-2}.

As reported previously,[8] time-resolved microwave photoconductivity measurements (TRMC) are based on changes in the complex permittivity of the MUT due to exposure to UV light. From the UV-Vis spectroscopy it is clear that any incident light of wavelength lower than 400 nm will be absorbed. This results in two changes that immediately effect the microwave properties of the MUT and therefore the entire circuit. First, free carriers are generated and these excess electrons and holes will increase the effective material conductivity (loss tangent) of nanotubes, which as a result impacts the microwave signal and changes the amplitude and the frequency of the power transferred through the MUT. As shown in Fig. 2, increase of the conductivity reduces the resonant frequency and amplitude of the signal. Secondly, some of these carriers will be trapped in defect states or surface states of the nanotube array becoming bound charges. Bound charges may exist in the material for minutes or hours before recombining and during this time they are more polarizable than the otherwise charge-neutral material. This buildup of bound charges from continued exposure to UV light will increase the permittivity of the material over time. Increased permittivity, reduces the resonant frequency and singal amplitude and are observed in longer time experiments presented in Fig. 5. The end result, namely an increasing conductivity and permittivity is consistent between simulation and experimental results (Fig. 4). The observed frequency and amplitude variation trend observed in this experiment match well with the predicted behviaour of the sensor in the simulation of Fig. 2. The time-constants of the resonant frequency (τ_{fr}) and resonant amplitude (τ_{Ar}) during the excitation time for different current level of UV-LED were extracted using a first order exponential response and are reported in Table 2.

Table 2. Resonant frequency and resonant amplitude time constants for excitation period in different bias current and light intensity power of UV-LED

Bias current (mA)	4	8	16	20	24	34	44	64	84	124	164	200
τ_{fr} (sec)	169	117	107	105	84	69	63	48	41	34	26	25
τ_{Ar} (sec)	242	143	117	84	83	62	56	53	49	45	44	44
Intensity Power (μW/cm^2)	7.94	25.8	70	113	137	199	260	382	504	747	993	1204

5 Discussion on limit of detection

To demonstrate the strength of the sensor as a very sensitive UV intensity detector, the UV-LED was driven by very low bias currents of 500 µA and 100 µA, which corresponded to 66.2 nW cm^{-2} and 1.96 nW cm^{-2} respectively. As the light intensity is reduced, it is observed that the system reaches the frequency noise level (no distinct frequency shift is observed) while the amplitude variation detection is still clear and evident. Since due to the generation and recombination states, the conductivity of the nanotubes is more impacted than the permittivity, the equivalent loss tangent changes observed by the microwave resonator are easier to measure for at light low levels. Loss tangent directly impacts the amplitude of the signal. Fig. 2 (b) also provides confirmation for the fact that loss tangent changes the amplitude of the signal more significantly than the resonant frequency.

The resonant amplitude transient responses to the targeted intensities are presented in Fig. 6a. A first order exponential fitting function was applied to the measured results to extract the excitation and recombination time-constants. The equation parameters are summarized in Table III for $A_r(t) = A_0 + A_1 e^{-(t-t0)/\tau}$ fitting function. The experiments were repeated 3-times each to demonstrate the reliability and repeatability of the results.

Table 3. Parameters of the fitting function for different UV-intensities and in excitation and recombination modes.

		A_0	A_1	t_0	τ	ΔA_r	COD(R^2)	Chi-sqr
66.2 nW/cm^2	Excitation	8.158	0.08	125	15418	0.06	0.998	7.3e-7
	Recombination	8.336	-0.1	26580	32268	0.06	0.998	1.8e-6
1.96 nW/cm^2	Excitation	8.235	0.052	1700	17028	0.035	0.997	3.6e-7
	Recombination	8.313	-0.065	23940	56027	0.035	0.998	2.7e-7

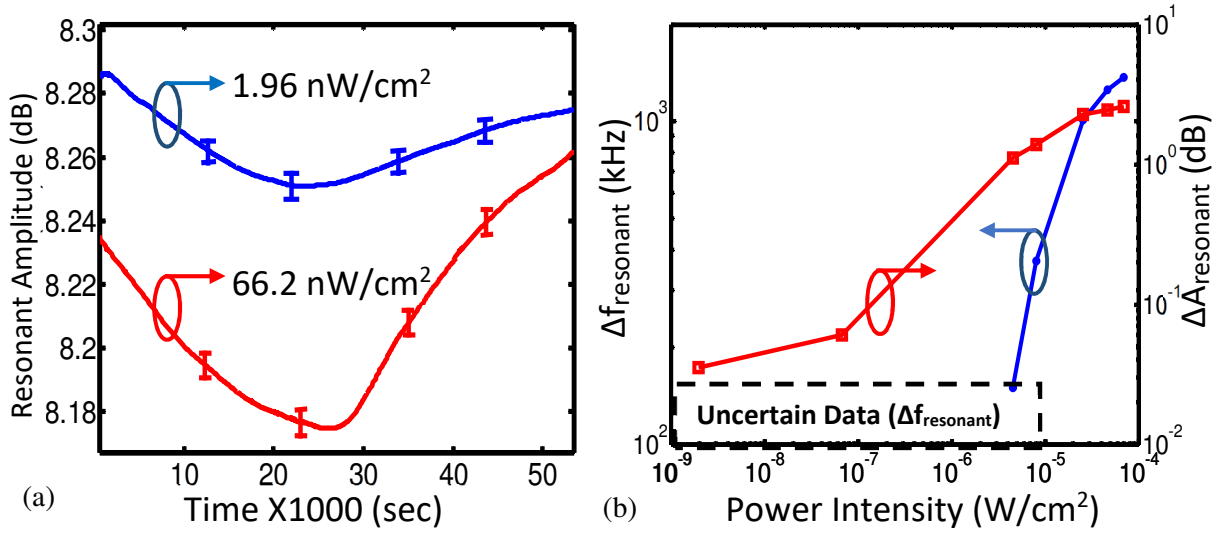

Fig. 6 (a) Transient response of the resonant amplitude for 1.96 and 66.2 nW/cm2 illumination power, (b) sensor response (resonant frequency and amplitude) regarding to different power intensities of UV-LED.

The curve fitting function $f_r(p) = f_0 + f_1 e^{-(p-p0)/\tau}$ in kHz, was applied to the resonant frequency response of the microwave sensor with respect to different power intensities of the UV-LED, where $f_0 = 1.39 \times 10^3$, $f_1 = -1.23 \times 10^3$, $p_0 = 4.56 \times 10^{-6}$ W cm^{-2} and $\tau = 1.83 \times 10^{-5}$ W cm^{-2} with COD(R^2) factor of 0.999. The change in resonant amplitude demonstrated a linear variation with respect to changes in the incident power intensity from the LED. The fitting function $A_r(p) = m \times p + n$ was applied to the resonant amplitude response in Fig. 6b (log scale) with the following parameters, m = 0.46, n =2.4 and COD(R^2) = 0.96. The fitting curve on resonant amplitude change confirmed an average sensitivity of 0.46 dB/decay of the sensor response with respect to intensity power of the UV-LED.

6 Conclusion

In this paper, a novel platform is introduced that combines active microwave resonator with anatase TiO_2 nanotubes for very low UV light sensing. Significantly high quality factor of the resonator enables ultra-high resolution sensing with minimum detection of as small as 1.96 nW/cm^2. The photoconductivity variations of nanotubes at the illumination and relaxation time impacts the effective complex permittivity observed by the microwave resonator which is used as UV light sensing signature. It is also observed that the amplitude of the signal transmission profile

is the most sensitive parameter that can be analyzed to obtain transient behaviour of the nanotubes, i.e. electron pair hole generation and recombination, and thus UV light quantification. The capability of such small light intensity detection using hybrid integrated circuits are mostly due to the unique high resolution microwave sensing platform. To our knowledge, this is the first time that microwave high resolution sensors are integrated with nanotubes and used in light sensing applications.

Conflicts of Interest

There are no conflicts to declare.

Acknowledgements

All authors thank NSERC for financial support. Daneshmand's group acknowledges Canada Research Chair program. B.D.W. was supported by a graduate student scholarship from Alberta Innovates Technology Futures. Some device fabrication and testing used research infrastructure made possible by a Leaders Opportunity Fund grant to K.S. and M.D. from the Canada Foundation for Innovation (CFI) and the Alberta Small Equipment Grants Program (SEGP). CMC Microsystem is also acknowledged for providing equipment and software support. We acknowledge use of the following facilities: the NRC-NINT Electron Microscopy Lab and the University of Alberta Nanofab.

References

1. S. Nakamura and H. Hashimoto, *IEEE Sens. J.*, 2015, **15**, 3675-3686.
2. M. H. Zarifi, P. Shariaty, M. Abdolrazzaghi, Z. Hashisho and M. Daneshmand, *Sens. Actuators, B*, 2016, **234**, 332-337.
3. J. Nohlert, T. Rylander and T. McKelvey, *IEEE T. Microw. Theory*, 2016, 1-13.
4. H. Choi, J. Naylon, S. Luzio, J. Beutler, J. Birchall, C. Martin and A. Porch, *IEEE T. Microw. Theory*, 2015, **63**, 3016-3025.
5. M. H. Zarifi and M. Daneshmand, *Appl. Phys. Lett.*, 2016, **108**, 232906-232906.
6. B. Wang, J. Long and K. Teo, *Sensors*, 2016, **16**, 150-150.
7. L. Benkhaoua, M. T. Benhabiles, S. Mouissat and M. L. Riabi, *IEEE Sens. J.*, 2016, **16**, 1603-1610.
8. M. H. Zarifi, A. Mohammadpour, S. Farsinezhad, B. D. Wiltshire, M. Nosrati, A. M. Askar, M. Daneshmand and K. Shankar, *J. Phys. Chem. C*, 2015, **119**, 14358-14365.

9. M. H. Zarifi, S. Farsinezhad, M. Abdolrazzaghi, M. Daneshmand and K. Shankar, *Nanoscale*, 2016, **8**, 7466-7473.
10. M. H. Zarifi, S. Farsinezhad, B. D. Wiltshire, M. Abdorrazaghi, M. Najia, P. Kar, M. Daneshmand and K. Shankar, *Nanotechnology*, 2016, **27**, 375201-375201.
11. M. H. Zarifi, M. Rahimi, M. Daneshmand and T. Thundat, *Sens. Actuators, B*, 2016, **224**, 632-639.
12. M. H. Zarifi, T. Thundat and M. Daneshmand, *Sens. Actuators, A*, 2015, **233**, 224-230.
13. M. Nick and A. Mortazawi, *IEEE T. Microw. Theory*, 2010, **58**, 1133-1139.
14. M. H. Zarifi, S. Farsinezhad, K. Shankar and M. Daneshmand, *IEEE Microw. Wirel. Co.*, 2015, **25**, 621-623.
15. M. H. Zarifi, P. Shariaty, Z. Hashisho and M. Daneshmand, *Sens. Actuators, B*, 2017, **238**, 1240-1247.
16. P. Kar, Y. Zhang, S. Farsinezhad, A. Mohammadpour, B. D. Wiltshire, H. Sharma and K. Shankar, *Chem. Commun.*, 2015, **51**, 7816-7819.
17. C. T. Yip, H. Huang, L. Zhou, K. Xie, Y. Wang, T. Feng, J. Li and W. Y. Tam, *Adv. Mater.*, 2011, **23**, 5624-5628.
18. A. Mohammadpour and K. Shankar, *J. Mater. Chem.*, 2010, **20**, 8474-8477.
19. G. Wang, J. Wang, Y. An and C. Wang, *Superlattices Microstruct.*, 2016, **100**, 290-295.
20. M. Guo, H. Su, J. Zhang, L. Liu, N. Fu, Z. Yong, H. Huang and K. Xie, *J. Power Sources*, 2017, **345**, 12-20.
21. Y. Zhang, S. Farsinezhad, B. D. Wiltshire, R. Kisslinger, P. Kar and K. Shankar, *Nanotechnology*, 2017, **28**, Art# 374001.
22. D. Regonini, C. R. Bowen, A. Jaroenworaluck and R. Stevens, *Mat. Sci. Eng. R*, 2013, **74**, 377-406.
23. P. Roy, S. Berger and P. Schmuki, *Angew. Chem., Int. Ed.*, 2011, **50**, 2904-2939.
24. J. Wang and Z. Lin, *Chem. Mater.*, 2008, **20**, 1257-1261.
25. T. Xia, C. Zhang, N. A. Oyler and X. Chen, *Adv. Mater.*, 2013, **25**, 6905-6910.
26. A. Mohammadpour, P. Kar, B. D Wiltshire, A. M Askar and K. Shankar, *Curr. Nanosci.*, 2015, **11**, 593-614.
27. X. Chen and S. S. Mao, *Chem. Rev.*, 2007, **107**, 2891-2959.
28. C. Wehrenfennig, C. M. Palumbiny, H. J. Snaith, M. B. Johnston, L. Schmidt-Mende and L. M. Herz, *J. Phys. Chem. C*, 2015, **119**, 9159-9168.
29. J. R. Jennings, A. Ghicov, L. M. Peter, P. Schmuki and A. B. Walker, *J. Am. Chem. Soc.*, 2008, **130**, 13364-13372.
30. C. Richter and C. A. Schmuttenmaer, *Nat Nano*, **5**, 769-772.
31. Q. Zhang, V. n. Celorrio, K. Bradley, F. Eisner, D. Cherns, W. Yan and D. J. Fermin, *J. Phys. Chem. C*, **118**, 18207-18213.
32. R. Mohammadpour, A. Iraji zad, A. Hagfeldt and G. Boschloo, *ChemPhysChem*, **11**, 2140-2145.
33. R. S. Chen, C. A. Chen, H. Y. Tsai, W. C. Wang and Y. S. Huang, *J. Phys. Chem. C*, 2012, **116**, 4267-4272.
34. L. K. Krehula, A. Papić, S. Krehula, V. Gilja, L. Foglar and Z. Hrnjak-Murgić, *Polym. Bull. (Berlin)*, 2017, **74**, 1387-1404.
35. T. Schmid, B. Baumann, M. Himmelsbach, C. W. Klampfl and W. Buchberger, *Anal. Bioanal. Chem.*, 2016, **408**, 1871-1878.
36. M. M. Badalà, A. Sciuto, G. Mannino, L. Renna and N. Costa, *J. Instrum.*, 2016, **11**, P10010-P10010.
37. J. Lähnemann, M. Den Hertog, P. Hille, M. a. de la Mata, T. Fournier, J. Schörmann, J. Arbiol, M. Eickhoff and E. Monroy, *Nano Lett.*, 2016, **16**, 3260-3267.
38. H. Chong, H. Yang, W. Yang, J. Zheng, M. Shang, Z. Yang, G. Wei and F. Gao, *J. Nanosci. Nanotechnol.*, 2016, **16**, 3796-3801.

39. X. Wang, Y. Zhang, X. Chen, M. He, C. Liu, Y. Yin, X. Zou and S. Li, *Nanoscale*, 2014, **6**, 12009-12017.
40. M. R. Alenezi, A. S. Alshammari, T. H. Alzanki, P. Jarowski, S. J. Henley and S. R. P. Silva, *Langmuir*, 2014, **30**, 3913-3921.
41. A. H. Adl, P. Kar, S. Farsinezhad, H. Sharma and K. Shankar, *RSC Adv.*, 2015, **5**, 87007-87018.
42. S. Lu, J. Qi, S. Liu, Z. Zhang, Z. Wang, P. Lin, Q. Liao, Q. Liang and Y. Zhang, *ACS Appl. Mater. Interfaces*, 2014, **6**, 14116-14122.
43. C. Soci, A. Zhang, B. Xiang, S. A. Dayeh, D. P. R. Aplin, J. Park, X. Y. Bao, Y. H. Lo and D. Wang, *Nano Lett.*, 2007, **7**, 1003-1009.
44. P. B. Myoung, C. Seong Rae, K. Jong-Woo, B. Sung-Doo and M. Jae, *Nanotechnology*, 2017, **28**, 225502-225502.
45. G. Jang, S. Jeong Lee, D. Lee, D. Lee, W. Lee and J.-M. Myoung, *J. Mater. Chem. C*, 2017, **5**, 4537-4542.